THE JOURNAL OF PHYSICAL CHEMISTRY A

Article

pubs.acs.org/JPCA

Spectroscopic Determination of Aerosol pH from Acid–Base Equilibria in Inorganic, Organic, and Mixed Systems

Published as part of The Journal of Physical Chemistry virtual special issue "Veronica Vaida Festschrift".

Rebecca L. Craig,[†] Lucy Nandy,[‡] Jessica L. Axson,[§] Cari S. Dutcher,[‡] and Andrew P. Ault*[,†,§]

[†]Department of Chemistry and [§]Department of Environmental Health Sciences, University of Michigan, Ann Arbor, Michigan 48109, United States

[‡]Department of Mechanical Engineering, University of Minnesota, Minneapolis, Minnesota 55455, United States

Supporting Information

ABSTRACT: Atmospheric aerosol acidity impacts key multiphase processes, such as acid-catalyzed reactions leading to secondary organic aerosol formation, which impact climate and human health. However, traditional indirect methods of estimating aerosol pH often disagree with thermodynamic model predictions, resulting in aerosol acidity still being poorly understood in the atmosphere. Herein, a recently developed method coupling Raman microspectroscopy with extended Debye–Hückel activity calculations to directly determine the acidity of individual particles (1–15 μm projected area diameter, average 6 μm) was applied to a range of atmospherically relevant inorganic and organic acid–base equilibria systems (HNO_3/NO_3^-, $HC_2O_4^-/C_2O_4^{2-}$, CH_3COOH/CH_3COO^-, and HCO_3^-/CO_3^{2-}) covering a broad pH range (−1 to 10), as well as an inorganic–organic mixture (sulfate-oxalate). Given the ionic strength of the inorganic solutions, the H^+ activity, $\gamma(H^+)$, yielded lower values (0.68–0.75) than the organic and mixed systems (0.72–0.80). A consistent relationship between increasing peak broadness with decreasing pH was observed for acidic species, but not their conjugate bases. Greater insight into spectroscopic responses to acid–base equilibria for more complicated mixtures is still needed to understand the behavior of atmospheric aerosols.

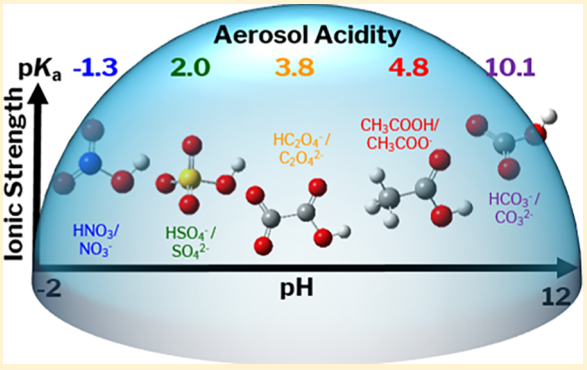

INTRODUCTION

Atmospheric aerosols impact both climate and human health, yet many of the chemical mechanisms occurring within aerosols remain poorly understood.[1] Many key multiphase chemical processes in aerosol particles are pH-dependent, such as secondary organic aerosol (SOA) formation,[2−11] which makes understanding aerosol acidity important for assessing the impact of aerosols on climate.[12] Specific pH-dependent processes include acid-catalyzed ring-opening reactions of epoxides (e.g., isoprene epoxydiol),[12−14] formation and hydrolysis of organosulfates and organic nitrates,[15−19] water uptake,[20,21] liquid–liquid phase separations,[22,23] and gas-particle partitioning.[24] One of the challenges for predicting the kinetics and overall importance of these processes is that methods to experimentally determine aerosol acidity are limited, but the available data suggest considerable variation between regions globally.[25−29] As an example, sulfate, which is formed from oxidation of $SO_{2(g)}$, is a large contributor to the acidity of aerosols, yet, despite decreasing atmospheric gaseous SO_2 emissions and subsequent condensed-phase sulfate concentrations in the southeast United States, aerosol pH has remained low (pH 0–2) over the past 15 years.[30] Considering the complex mixture of emissions and atmospheric reactions that ultimately determine aerosol pH, more refined techniques for measuring aerosol pH are necessary to evaluate the overall impact on atmospheric multiphase chemical processes.

Until recently, evaluation of aerosol pH has been primarily through indirect filter-based measurements or proxy methods, such as ion balance, molar ratio, phase partitioning, or thermodynamic equilibrium models.[25] Upon examination of these methods, Hennigan et al.[25] concluded that thermodynamic models and the phase partitioning method provide the most accurate estimations of aerosol pH. Thermodynamic equilibrium models, such as ISORROPIA-II[31] and E-AIM,[32,33] use temperature, relative humidity (RH), and measured concentrations of aerosol species and gas-phase precursors to predict concentrations of chemical species in both gas and aerosol phases, aerosol water, and aerosol pH. These models have been increasingly applied to evaluate aerosol acidity during several field campaigns, including MILAGRO,[25] SOAS,[26] WINTER,[27] and CALNEX,[28] as well as recent haze events in China.[29] The phase partitioning method uses measurements of

Received: May 30, 2017
Revised: June 29, 2017
Published: July 10, 2017

DOI: 10.1021/acs.jpca.7b05261
J. Phys. Chem. A 2017, 121, 5690−5699

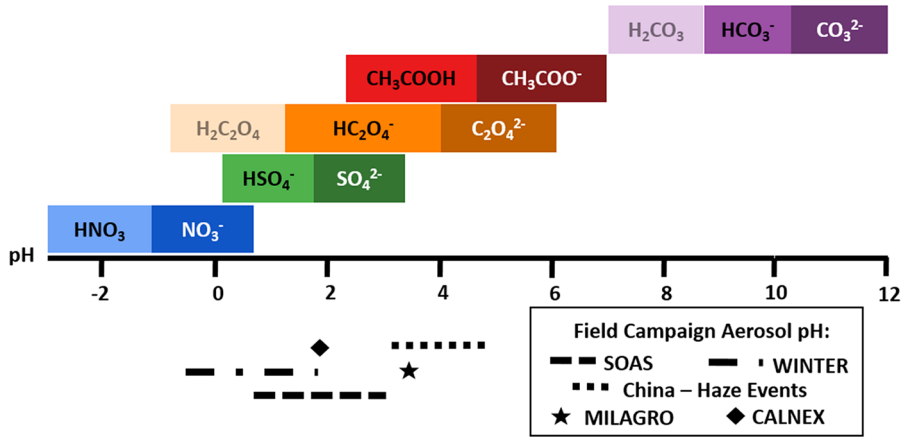

Figure 1. Schematic showing dominant species present as a function of pH for each acid–base system studied, as well as a comparison to the aerosol pH predicted by thermodynamic models for several field campaigns. $H_2C_2O_4$ and H_2CO_3 are included but cannot be quantified with this method.

gas- and aerosol-phase components to estimate aerosol pH from the phase partitioning of semivolatile compounds, such as HNO_3/NO_3^- and NH_3/NH_4^+.[34,35] Limitations for both the thermodynamic models and phase partitioning method include sensitivity to input values and the uncertainty associated with those measurements.[25,26,34] Additionally, the phase partitioning method follows the assumption that the gas-particle phase system is at equilibrium, which is not necessarily accurate, particularly in conditions of high ionic strength or low liquid water content common in the atmosphere.[34,36−39] In comparison to the phase partitioning method, estimations of aerosol pH using filter-based measurements[34,40,41] and the ion balance[42−44] and molar ratio[45,46] proxy methods are all associated with higher degrees of uncertainty and disagreement with model predictions. These disagreements are mainly due to challenges associated with predicting $[H^+]$, since it is not conserved relative to other chemical species that are more easily measured.[25] For filter-based measurements, uncertainty can also be attributed to sampling artifacts.[47] Additional limitations of the ion balance and molar ratio methods include lack of consideration for aerosol liquid water content and ion activity coefficients, exclusion of organic acids, and inability to differentiate types of H (e.g., whether or not H^+ is a dissociated ion), though all of these factors are important for determining aerosol pH.[25,34,43,44,48]

In contrast to these indirect and proxy methods, Rindelaub et al.[49] recently developed a novel method utilizing Raman microspectroscopy, a technique that has been increasingly applied for analysis of individual laboratory and ambient particles in recent years.[50−56] Wren and Donaldson[57,58] have also used a spectroscopic technique to study the pH of air–ice interfaces, but it involves indirect measurement through glancing-angle laser-induced fluorescence in conjunction with pH-sensitive fluorescent dyes. Rindelaub et al. directly measured the pH of laboratory-generated $MgSO_4–H_2SO_4$ aerosol particles, a common seed aerosol used in SOA chamber studies.[17] Measured peak areas of the $\nu_s(SO_4^{2-})$ and $\nu_s(HSO_4^-)$ vibrational modes were used to determine SO_4^{2-} and HSO_4^- ion concentrations, respectively.[49] The acid (HSO_4^-) and conjugate base (SO_4^{2-}) concentrations were then used, along with activity coefficients determined via the extended Debye–Hückel relationship and the acid dissociation constant (K_a), to calculate $[H^+]$ and pH.[49] This method overcomes limitations of the previously discussed proxy methods, such as differentiating types of H^+ and accounting for aerosol liquid water ccontent. This method has potential to provide insight into chamber and ambient aerosol particle pH, which would be a valuable comparison to current predictions of aerosol pH, but has only been applied to one relatively simple acid–base equilibrium system over a limited pH range.[49]

In this work, the spectroscopic method described above for determining aerosol particle pH[49] has been applied to inorganic and organic acids with a range of pK_a values in individual aerosol particles (Figure 1). These systems include nitric acid/nitrate $(HNO_3/NO_3^-$, pK_a −1.3), bioxalate/oxalate $(HC_2O_4^-/C_2O_4^{2-}$, pK_a 3.81), acetic acid/acetate $(CH_3COOH/CH_3COO^-$, pK_a 4.76), and bicarbonate/carbonate $(HCO_3^-/CO_3^{2-}$, pK_a 10.30).[59,60] These systems cover a wide pH range, including the typical range for atmospheric aerosols (pH −0.5 to +5).[25−29] The aerosol acidity predicted by thermodynamic models for several field campaigns are also indicated in Figure 1 and fall well within the range of several of the acid–base systems.[26−29] A large fraction of aerosols are a mixture of inorganic and organic species; thus, in addition to these single acid–conjugate base systems, a two-component mixture of bisulfate/sulfate $(HSO_4^-/SO_4^{2-}$, pK_a 2.0)[59] and $HC_2O_4^-/C_2O_4^{2-}$ was characterized to study the impact of increasing chemical complexity of the particles on the spectroscopic pH measurements. Observations of ion behavior in terms of ionic strength, H^+ activity, and solvent interactions were also made for each acid–base system. This work responds to a recent call for more physical chemistry approaches to single particle measurements[61] and will enable future studies to improve understanding of pH of more chemically complex aerosol particles.

METHODS

Standard solutions were prepared using 18.3 MΩ Milli-Q water and the following chemicals: ammonium oxalate $((NH_4)_2C_2O_4)$, sodium acetate $(NaCH_3COO)$, sodium bicarbonate $(NaHCO_3)$, sodium nitrate $(NaNO_3)$, hydrochloric acid (HCl), nitric acid (HNO_3), and sulfuric acid (H_2SO_4) (Sigma-Aldrich); oxalic acid $(H_2C_2O_4)$ (Acros Organics); ammonium sulfate $((NH_2)_2SO_4)$ (Alfa Aesar); acetic acid (HCH_3COO) (Fisher Scientific); and sodium carbonate (Na_2CO_3) (JT Baker Chemical Co.). All chemicals were greater than 98.0% purity and used without further purification. To create a solution for each acid–base system, a salt containing the base was dissolved

DOI: 10.1021/acs.jpca.7b05261
J. Phys. Chem. A 2017, 121, 5690−5699

Table 1. Composition and pH of Solutions Used to Generate Aerosol Particles, along with Vibrational Modes Corresponding to the Acid and Conjugate Base, for Each Acid−Base System

		solution composition		acid		base	
acid−base system	bulk solution pH	salt	acid	mode	freq[a] (cm^{-1})	mode	freq[a] (cm^{-1})
HNO_3/NO_3^-	<0[b]	$NaNO_3$	HNO_3	$\nu_s(HNO_3)$	1306	$\nu_s(NO_3^-)$	1047
$HC_2O_4^-/C_2O_4^{2-}$	3.63	$(NH_4)_2C_2O_4$	HCl	ν(C−C) $HC_2O_4^-$	873	ν(C−C) $C_2O_4^{2-}$	907
	3.97						
HCH_3COO/CH_3COO^-	3.92	$NaCH_3COO$	HCl	ν(C−C) CH_3COO	890	ν(C−C) CH_3COO^-	927
HCO_3^-/CO_3^{2-}	10.47	Na_2CO_3	HCl	$\nu_s(HCO_3^-)$	1019	$\nu_s(CO_3^{2-})$	1067
HSO_4^-/SO_4^{2-} & $HC_2O_4^-/C_2O_4^{2-}$	0.39	$(NH_4)_2SO_4$, $(NH_4)_2C_2O_4$	H_2SO_4	$\nu_s(HSO_4^-)$	1053	$\nu_s(SO_4^{2-})$	983
	0.83						
	3.58			ν(C−C) $HC_2O_4^-$	873	ν(C−C) $C_2O_4^{2-}$	907
	3.99						

[a]Frequencies identified from calibration of standard compounds. [b]pH below measurement range of pH probe.

in solution and then mixed with a strong acid to control the pH. Bulk solution pH was measured by a pH probe (AP110, accumet Portable). Table 1 lists the pH, salt, and acid comprising each solution used to generate aerosol particles. Concentration values for each solution are provided in Table S1. Aerosols were generated from solutions using a Collison nebulizer (atomizer) operated with HEPA-filtered air and then impacted onto quartz substrates (Ted Pella, Inc.) using a Microanalysis Particle Sampler (MPS-3, California Measurements, Inc.). For the HCO_3^-/CO_3^{2-} system, generated aerosols were passed through two diffusion dryers prior to impaction to remove liquid-phase water and increase the concentration of analytes in individual particles (concentration increased by a factor of ∼100 on average). Particles from Stage 1 of the MPS (>2.8 μm equivalent aerodynamic diameter cut-point) were analyzed to ensure particles were larger than the Rayleigh diffraction limit (0.36 μm) and spot size (0.72 μm) for the Raman spectrometer (0.9 N.A. objective with a 532 nm laser). The projected area diameter (d_{pa}) size range for particles studied is determined by optical imaging and refers to the diameter of a circle with the same projected area as the particle. For the particles in this study, d_{pa} ranged from 1−15 μm, with an average of 6.3 μm. These d_{pa} values are larger than aerodynamic or geometric diameters of the particles prior to impaction due to spreading upon impaction.

Raman spectra for individual impacted particles were collected using a LabRAM HR Evolution Raman microspectrometer (Horiba, Ltd.) equipped with a Nd:YAG laser source (50 mW, 532 nm) and CCD detector and coupled with a confocal optical microscope (100× 0.9 N.A. SLMPlan N Olympus objective). The instrument was calibrated against the Stokes Raman signal of pure Si at 520 cm^{-1} using a silicon wafer standard. Spectra from 500 to 1400 cm^{-1} were acquired for 5 s with three accumulations for the inorganic acid systems and 15 s with three accumulations for the organic acid systems and the mixture. A 600 groove/mm diffraction grating yielded spectral resolution of ∼1.7 cm^{-1}. Spectra were collected at ambient temperature and relative humidity (RH), monitored with an RH sensor (EK-H5, Sensiron). A 2 μL droplet of each solution was also analyzed to compare bulk solution spectra with those of the particles.

The pH of individual aerosol particles was determined using the method described by Rindelaub et al.[49] Briefly, integrated peak areas of the vibrational modes corresponding to an acid (HA) and conjugate base (A^-) for each acid−base system were related to concentration using calibration curves (Figures S1−S5). The vibrational modes analyzed for each acid−base system are included in Table 1. The concentration of other ions present in the particle (those not directly involved in the acid−base equilibrium) were determined from the ratio of [ion]/[acid + conjugate base] (Table S1). Once the concentration of all ions present was determined, ionic strength (I) was calculated via eq 1, where C_i and z_i represent the concentration of each ion and its corresponding charge, respectively.

$$I = \frac{1}{2}\sum C_i z_i^2 \tag{1}$$

Molality units were used for concentration of each species, determined by converting molarity to molality using the density of the solution mixture. The solution densities were found by using the Laliberté model,[62] and were iteratively solved during molality conversions. Since the density calculations required concentrations of each solute in the solution mixture, the equivalent concentrations of each cation and anion were found by Clegg's equivalent fraction method,[63] which assumes that all possible combinations of cation and anion are present as solute components.

Then the extended Debye−Hückel relationship (eq 2) was applied to calculate the activity coefficient for each species in the acid−base equilibrium. In the extended Debye−Hückel relationship, A and B are constants characteristic of the solvent (water), and $\mathring{a}_i$ is the effective diameter of the ion in solution.[64,65] Values for the constants used in the extended Debye−Hückel relationship can be found in Table S2.

$$-\log \gamma_i = \frac{A z_i^2 \sqrt{I}}{1 + \mathring{a}_i B \sqrt{I}} \tag{2}$$

The concentrations of acid and conjugate base, their respective activity coefficients, and the acid dissociation constant K_a were then used to calculate $[H^+]$ (eq 3) and finally pH (eq 4).

$$K_a = \frac{a_{H^+} * a_{A^-}}{a_{HA}} = \frac{([H^+]*\gamma_{H^+})([A^-]*\gamma_{A^-})}{[HA]*\gamma_{HA}} \tag{3}$$

$$pH = -\log(a_{H^+}) = -\log(\gamma_{H^+}*[H^+]) \tag{4}$$

DOI: 10.1021/acs.jpca.7b05261
J. Phys. Chem. A 2017, 121, 5690−5699

Note that an iterative method is needed to solve eqs 1−3, since the value of $[H^+]$ is not known and is needed in the calculation of ionic strength and activity coefficients. As with the density calculations (discussed after eq 1), Clegg's equivalent fraction method[63] was used to find the first initial value for $[H^+]$. This value is then used to solve for ionic strength (eq 1) and subsequently the activity coefficients (eq 2). Using the activity coefficients, eq 3 is applied to calculate a new value for $[H^+]$. The initial value for $[H^+]$ is then iteratively changed until it equals that from the eq 3 calculations.

RESULTS AND DISCUSSION

Aerosol particle pH was evaluated for each acid and conjugate base system and is discussed in terms of inorganic acid systems (HNO_3/NO_3^- and HCO_3^-/CO_3^{2-}), organic acid systems ($HC_2O_4^-/C_2O_4^{2-}$ and CH_3COOH/CH_3COO^-), and a mixed inorganic−organic system ($HC_2O_4^-/C_2O_4^{2-}$ with HSO_4^-/SO_4^{2-}). Figure 2 shows the relative fraction of each inorganic

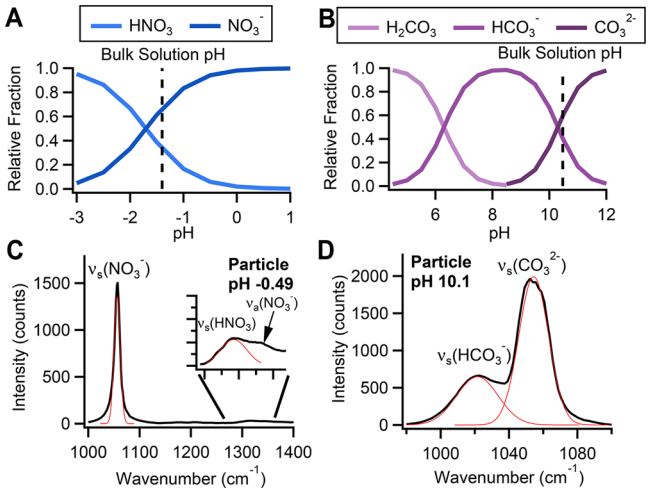

Figure 2. Relative fraction as a function of pH for (A) nitric acid equilibrium and (B) carbonic acid and bicarbonate equilibrium, with the pH of the bulk solutions used to generate aerosol particles indicated by the dashed line. Raman spectra for a (C) HNO_3/NO_3^- aerosol particle pH −0.49 and a (D) HCO_3^-/CO_3^{2-} aerosol particle pH 10.1. Red lines indicate Gaussian peak fits.

species as a function of pH for the nitric acid and carbonic acid equilibriums, respectively. Since the pH was too low to be measured accurately with the pH probe, the pH of the bulk solution used to generate aerosol particles for the HNO_3/NO_3^- system was calculated to be between −1.1 and −1.4, based on the concentration of ions in solution. The pH of HNO_3/NO_3^- aerosol particles when calculated using the extended Debye−Hückel model varied from −1.2 to 0.090, with an average of −0.48. A histogram showing the pH for all particles measured (for the HNO_3/NO_3^- system and all systems discussed later) is included in the Supporting Information. The Raman spectrum of a representative HNO_3/NO_3^- particle (pH = −0.49, d_{pa} = 9.9 μm) is shown in Figure 2C, with the vibrational modes that were used to determine $[NO_3^-]$ and $[HNO_3]$ identified as $\nu_s(NO_3^-)$[66,67] at 1057 cm^{-1} and $\nu_s(HNO_3)$[68,69] at 1313 cm^{-1}, respectively. In the inset, the shoulder of the $\nu_s(HNO_3)$ mode at 1344 cm^{-1} was attributed to the $\nu_a(NO_3^-)$ mode.[66,67] As can be seen by the low intensity of the $\nu_s(HNO_3)$ mode relative to the $\nu_s(NO_3^-)$ mode, nitric acid was not conserved in the particle phase, a phenomenon that will be discussed further later. For comparison with an alternative prediction of pH, the multilayer adsorption isotherm-based model from Dutcher et al.[70] was also used to determine the molalities and activities of the solutes present, and subsequently the activity of H^+ and pH. With the Dutcher model, particle pH values were closer than the values from extended Debye−Hückel model to the calculated pH values of the HNO_3/NO_3^- bulk solution, ranging from −1.4 to −0.88, with an average pH of −1.2. The pH of the particle corresponding to the Raman spectrum shown in Figure 2C was calculated with the Dutcher model to be −1.17.

The measured pH of the bulk solution used to generate aerosol particles for the HCO_3^-/CO_3^{2-} system was 10.47. HCO_3^-/CO_3^{2-} aerosol particles varied in pH from 9.9 to 10.4, with an average of 10.1. The $\nu_s(HCO_3^-)$ vibrational mode[71] at 1023 cm^{-1} and $\nu_s(CO_3^{2-})$ vibrational mode[71] at 1052 cm^{-1} that were used to determine $[HCO_3^-]$ and $[CO_3^{2-}]$, respectively, are shown in the Raman spectrum of a representative HCO_3^-/CO_3^{2-} particle (pH = 10.1, d_{pa} = 4.1 μm) in Figure 2D. The H_2CO_3/HCO_3^- equilibrium could not be studied, due to the equilibrium between aqueous phase H_2CO_3 with CO_2 and H_2O.[72]

For the organic acids, the relative fractions of each species as a function of pH in the oxalic acid and acetic acid equilibriums are shown in Figure 3A,B, respectively. $HC_2O_4^-/C_2O_4^{2-}$

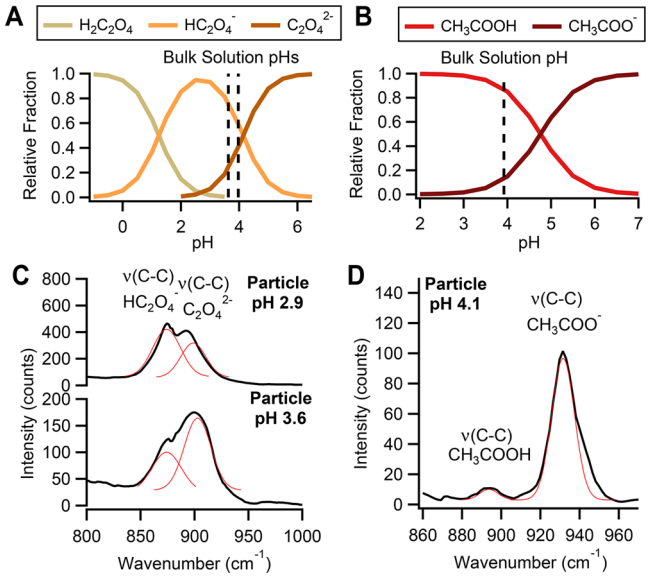

Figure 3. Relative fraction as a function of pH for (A) oxalic acid and bioxalate equilibrium and (B) acetic acid equilibrium, with the pH of the bulk solutions used to generate aerosol particles highlighted by the dashed line. Raman spectra for (C) $HC_2O_4^-/C_2O_4^{2-}$ aerosol particles pH 2.9 and 3.6 and (D) a CH_3COOH/CH_3COO^- aerosol particle pH 4.1. Red lines indicate Gaussian peak fits.

aerosol particles were atomized from two bulk solutions, with measured pH values of 3.63 and 3.97, respectively. Aerosol particle pH varied from 2.4 to 3.8 with an average of 3.0 and from 2.8 to 3.9 with an average of 3.3 for $HC_2O_4^-/C_2O_4^{2-}$ particles generated from the respective low- and high-pH bulk solutions. Raman spectra for two representative $HC_2O_4^-/C_2O_4^{2-}$ particles (pH = 2.9, d_{pa} = 15.0 μm and pH = 3.6, d_{pa} = 8.0 μm) are shown in Figure 3C. $[HC_2O_4^-]$ was determined from the $HC_2O_4^-$ ν(C−C) mode[73] at 876 cm^{-1}, and $[C_2O_4^{2-}]$ was determined from the $C_2O_4^{2-}$ ν(C−C) mode[74,75] at 899

DOI: 10.1021/acs.jpca.7b05261
J. Phys. Chem. A 2017, 121, 5690−5699

cm^{-1}. Under appropriately acidic conditions, $H_2C_2O_4$ can be identified by its ν(C−C) mode[76] at 850 cm^{-1} (Figure S7). However, close proximity to the ν(C−C) mode of $HC_2O_4^-$ makes it difficult to fit the two modes accurately enough to determine their respective ion concentrations, thus limiting the use of the $H_2C_2O_4/HC_2O_4^-$ equilibrium system with this method for determining aerosol particle pH.

For the CH_3COOH/CH_3COO^- equilibrium system, particles were generated from a bulk solution with a measured pH of 3.92, yielding aerosol particle pH values of 3.8 to 4.2, with an average of 4.0. The Raman spectrum of a representative CH_3COOH/CH_3COO^- particle (pH = 4.1, d_{pa} = 4.4 μm) is shown in Figure 3D, with the CH_3COOH ν(C−C) mode[77,78] used to calculate [CH_3COOH] identified at 892 cm^{-1} and the CH_3COO^- ν(C−C) mode[75] used to calculate [CH_3COO^-] identified at 931 cm^{-1}. Note that CH_3COOH measurements are most likely of acetic acid clusters, as CH_3COOH molecules can form dimers through hydrogen-bonding interactions in aqueous environments.[79] Similar to nitric acid, low intensity of the ν(C−C) mode for CH_3COOH relative to CH_3COO^- indicates less acetic acid is present in the particle phase due to gas-particle partitioning, and will be discussed in detail later.

The final set of particles was composed of both the $HC_2O_4^-/C_2O_4^{2-}$ and HSO_4^-/SO_4^{2-} equilibrium systems. Figure 4A shows the relative fraction of all species for both equilibrium systems as a function of pH. Particles were atomized from four bulk solutions of different pH values, namely, −0.39, 0.83, 3.58, and 3.99. For particles generated from the two lower pH solutions, the HSO_4^-/SO_4^{2-} equilibrium was used to determine pH. Particle pH ranged from 0.91 to 1.3 with an average of 1.2 for the lowest pH set (bulk solution pH 0.39) and 1.5 to 1.8 with an average of 1.6 for the higher pH set (bulk solution pH 0.83). For particles generated from the two higher pH solutions, the $HC_2O_4^-/C_2O_4^{2-}$ equilibrium was used to determine pH. Particle pH ranged from 3.6 to 4.7 with an average of 4.1 for the lower pH set (bulk solution pH 3.58) and 3.3 to 4.9 with an average of 3.7 for the higher pH set (bulk solution pH 3.99). Figure 4B shows spectra of a representative particle for which the HSO_4^-/SO_4^{2-} equilibrium was used to determine the pH (pH = 1.5, d_{pa} = 8.8 μm) and a representative particle for which the $HC_2O_4^-/C_2O_4^{2-}$ equilibrium was used to determine the pH (pH = 3.6, d_{pa} = 8.3 μm). Figure 4C shows the same spectra, focused closer on the spectral regions where the vibrational modes corresponding to the $HC_2O_4^-/C_2O_4^{2-}$ system and HSO_4^-/SO_4^{2-} system are located. Raman spectra of a representative particle (pH = 1.2, d_{pa} = 8.1 μm) generated from the pH 0.38 solution and a representative particle (pH = 3.9, d_{pa} = 4.4 μm) generated from the pH 3.58 solution are also shown in Figure 4C. For the HSO_4^-/SO_4^{2-} system, the $\nu_s(SO_4^{2-})$ and $\nu_s(HSO_4^-)$ modes were identified at 983 and 1050 cm^{-1}, respectively, and used to determine [SO_4^{2-}] and [HSO_4^-].[49,66] At the low pH values, all oxalate species were present in the form of oxalic acid, and thus the ν(C−C) mode[76] of $H_2C_2O_4$ at 850 cm^{-1} was used to determine [$H_2C_2O_4$], which was included in calculations of ionic strength. For the $HC_2O_4^-/C_2O_4^{2-}$ system, the same ν(C−C) modes for $HC_2O_4^-$ and $C_2O_4^{2-}$ discussed previously for particles composed of only the $HC_2O_4^-/C_2O_4^{2-}$ equilibrium were used to determine pH. At the high pH values, all sulfate species present were in the form of sulfate, and thus the $\nu_s(SO_4^{2-})$ mode was used to determine [SO_4^{2-}] and incorporated into the calculations of ionic strength. Aerosol particle pH for particles composed of only $HC_2O_4^-/C_2O_4^{2-}$ was, on average, lower in comparison to particles of $HC_2O_4^-/C_2O_4^{2-}$ and HSO_4^-/SO_4^{2-} mixed composition, despite similar pH bulk solutions used to generate particles and using the $HC_2O_4^-/C_2O_4^{2-}$ equilibrium to calculate pH for both systems. This phenomenon can be explained by differences in particle ionic strength and H^+ activity and will be discussed later. Successful determination of pH for these mixed system particles shows the potential for this method to be applied to aerosol particles of more complex chemical compositions, potentially even ambient aerosol particles if distinguishable modes for an acid and its conjugate base are present and measurable.

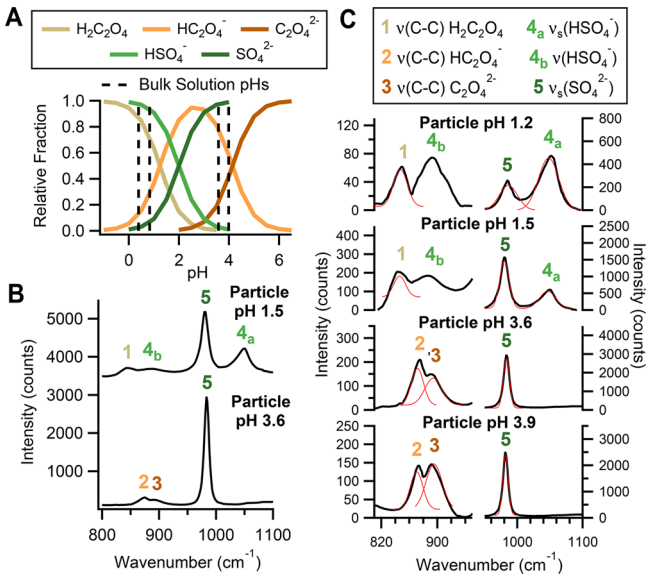

Figure 4. (A) Relative fraction as a function of pH for oxalic acid and bioxalate equilibrium and bisulfate equilibrium, with the pH of the bulk solutions used to generate oxalate−sulfate mixed aerosol particles highlighted by the dashed lines. (B) Full Raman spectra for $HC_2O_4^-/C_2O_4^{2-}$ and HSO_4^-/SO_4^{2-} mixed aerosol particles pH 1.5 and 3.2. (C) Raman spectra for $HC_2O_4^-/C_2O_4^{2-}$ and HSO_4^-/SO_4^{2-} aerosol particles pH 1.2, 1.5, 3.6, and 3.9 focused on spectral regions where ν(C−C) $HC_2O_4^-$, ν(C−C) $C_2O_4^{2-}$, $\nu_s(HSO_4^-)$, and $\nu_s(SO_4^{2-})$ are present. Red lines indicate Gaussian peak fits.

As mentioned previously in the discussions of the HNO_3/NO_3^- and CH_3COOH/CH_3COO^- equilibrium systems, HNO_3 and CH_3COOH are not conserved in the generated aerosol particles relative to their respective conjugate bases due to gas-particle partitioning. To further explore this phenomenon, Figure 5 shows a comparison of spectra of the HNO_3/NO_3^- and CH_3COOH/CH_3COO^- particles to spectra of the bulk solutions from which the particles were generated. The intensity of the vibrational modes corresponding to the acid for both systems is significantly larger in the bulk solution than in the particle; thus, the [acid]/[base] ratio in the bulk solution is larger than that of the particle. This indicates nitric acid and acetic acid are partitioning from the particle to gas phase during the atomization process, most likely due to quicker loss of vapor because of increased surface-to-volume ratio for the aerosol particles versus the droplets and/or heating from the laser. Nitric acid and acetic acid exhibit this behavior more than oxalic acid and the other ion compounds because of their higher volatility. The value for the Henry's Law constant (k_H°) for nitric acid and acetic acid is ~2×10^3 and ~4×10^1 mol m^{-3} Pa^{-1}, respectively, in contrast to the larger k_H° of ~6×10^6

DOI: 10.1021/acs.jpca.7b05261
J. Phys. Chem. A 2017, 121, 5690−5699

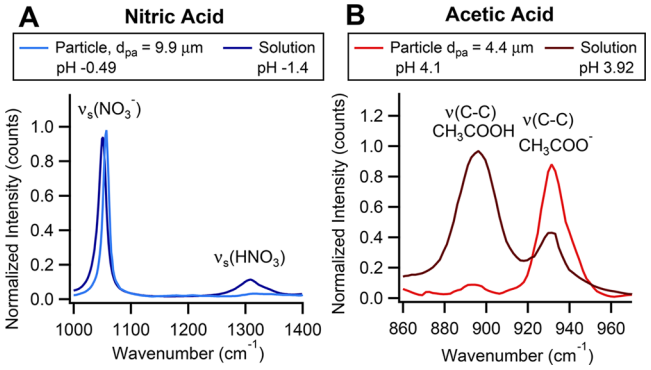

Figure 5. Raman spectra of a representative particle and the bulk solution for the (A) HNO_3/NO_3^- and (B) CH_3COOH/CH_3COO^- equilibrium systems. The spectra for the HNO_3/NO_3^- system were normalized to the $\nu_s(NO_3^-)$ mode, and the spectra for the CH_3COOH/CH_3COO^- system were normalized to the ν(C−C) mode of CH_3COO^-.

mol m^{-3} Pa^{-1} of oxalic acid.[80] A limited number of particles was analyzed for the CH_3COOH/CH_3COO^- system, due to challenges associated with partitioning of CH_3COOH to the gas phase. For comparison, Raman spectra of bulk solutions and particles for the $HC_2O_4^-/C_2O_4^{2-}$ system and the $HC_2O_4^-/C_2O_4^{2-}$ and HSO_4^-/SO_4^{2-} mixed system that did not exhibit this partitioning behavior are shown in Figure S8. The observation of decreased [acid]/[base] for aerosol particles for the HNO_3/NO_3^- and CH_3COOH/CH_3COO^- equilibrium systems could have implications for size-dependent particle acidity and particle phase reactions, such as acid-displacement in mixed sea salt and weak organic acid particles.[81]

In addition to measuring the pH of aerosol particles for each of these systems, trends were observed for H^+ activity coefficient $\gamma(H^+)$ in relation to ionic strength and aerosol particle pH relative to the broadness of the vibrational modes analyzed. Across all of the acid−base systems, there is a negative relationship for $\gamma(H^+)$ as a function of ionic strength (Figure 6), with more $\gamma(H^+)$ sensitivity at lower ionic strength.

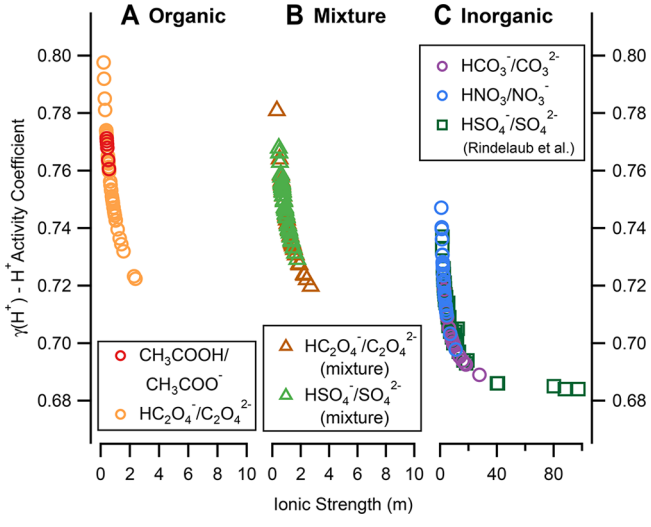

Figure 6. H^+ activity coefficient ($\gamma(H^+)$) as a function of ionic strength for each organic (A), mixture (B), and inorganic (C) acid−base system. Data for the HSO_4^-/SO_4^{2-} equilibrium from Rindelaub et al.[49] is also included for comparison. Note the differing scales for ionic strength.

However, the inorganic systems tend to have larger, more varied ionic strength with lower, less variable $\gamma(H^+)$. The inverse holds for the organic systems, which show larger, more varied $\gamma(H^+)$ with smaller and less variability in ionic strength. As mentioned earlier, even though particles were generated from bulk solutions of similar pH and the $HC_2O_4^-/C_2O_4^{2-}$ system was used to determine pH, particles composed of only $HC_2O_4^-/C_2O_4^{2-}$ had lower average pH than particles of $HC_2O_4^-/C_2O_4^{2-}$ and HSO_4^-/SO_4^{2-} mixed composition (average aerosol particle pH 3.2 and 4.0, respectively). Because of the inorganic component in the $HC_2O_4^-/C_2O_4^{2-}$ and HSO_4^-/SO_4^{2-} mixed particles, their $\gamma(H^+)$ was lower, thus decreasing the activity of H^+, making the particles less acidic. This observation supports that ion behavior in mixed organic and inorganic particles is dictated by contributions from all chemical species present.

In addition to the relationship between $\gamma(H^+)$ and ionic strength, aerosol particle pH as a function of peak broadness (full width at half-maximum−fwhm) was explored (Figure 7).

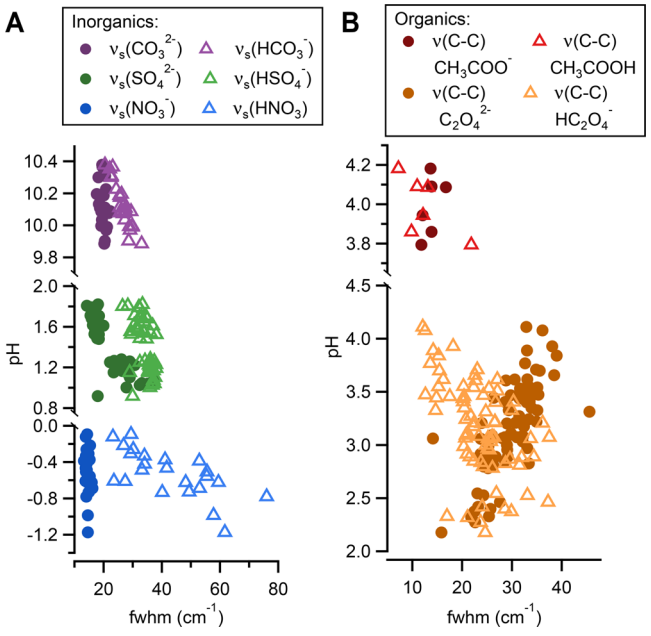

Figure 7. Aerosol particle pH as a function of the fwhm for (A) inorganic acids and bases and (B) organic acids and bases.

For vibrational modes corresponding to both the inorganic and organic acids, fwhm increased as particles became more acidic. The broadening of these modes may be attributed to different solvent binding conformations that occur as pH decreases and hydrogen bonding increases.[82] In the presence of more H_3O^+ ions and increased hydrogen bonding, there may be multiple solvent conformations, each with slightly different energies that form, leading to a broader peak that encompasses all of these variations in structure. The correlation (r) values for this trend are $\nu_s(HCO_3^-)$, −0.927; $\nu_s(HSO_4^-)$, −0.532; $\nu_s(HNO_3)$, −0.729; ν(C−C) CH_3COOH, −0.683; and ν(C−C) $HC_2O_4^-$, −0.513. Although there is a relatively strong correlation between aerosol particle pH and fwhm for ν(C−C) CH_3COOH, it is difficult to confidently identify a relationship due to the limited number of data points. A second aspect of pH versus peak width worth commenting on is the greater magnitude of broadening for the nitric acid peak

DOI: 10.1021/acs.jpca.7b05261
J. Phys. Chem. A 2017, 121, 5690−5699

versus the bicarbonate peak, which is attributed to significantly higher H_3O^+ concentration at pH −1 versus 10.

Additionally, note that the correlation between aerosol particle pH and fwhm of the vibrational mode corresponding to the acid species is not quite as strong for $\nu_s(HSO_4^-)$, −0.532 and ν(C−C) $HC_2O_4^-$, −0.513. For HSO_4^-, this could be due to the extra oxygen atom (four oxygen compared to two or three of the other acid species), which creates more resonance and increases the electron density, thus reducing the impact of hydrogen bonding on the symmetric S−O stretch and limiting broadening of its peak in the Raman spectra. Comparison with results from Rindelaub et al.[49] (Figure S9) shows a slightly stronger correlation between aerosol particle pH and $\nu_s(HSO_4^-)$ peak broadness (r = −0.659). For $HC_2O_4^-$, the impact of hydrogen bonding on peak fwhm is much less pronounced, since the analyzed vibrational mode corresponds to the C−C stretch of the backbone of the dicarboxylic acid, rather than a stretch containing an oxygen atom. However, according to density functional theory calculations (see Supporting Information for details on calculations), the ν(C−C) stretch is weakly coupled to the δ(O−C−O) bend, which is influenced by protonation and subsequent hydrogen bonding with decreasing pH.

In contrast to the acid species, for the inorganic base species, there was no correlation between aerosol particle pH and peak broadness. This observation is tentatively attributed to fewer solvent bonding conformations being possible for the more symmetric molecules, resulting in a consistently sharper peak. For the organic bases, the peak became narrower with decreasing pH, which could be due to increased concentration of the base species (oxalate or acetate) with decreasing pH, resulting in a more intense, and thus broader, peak. Because the ν(C−C) stretch for the organic base species is inherently broader than the symmetric stretch of the inorganic base species, this trend of increasing pH and ion concentration leading to increased peak broadness is only observed for the organic base species, though this is speculative, and further work is needed to explain this phenomenon. While there may appear to be a relationship between aerosol particle pH and peak fwhm for $\nu_s(SO_4^{2-})$, this is an artifact of analyzing two samples with two distinctly different pH values and thus two different populations of sulfate. When compared with results from Rindelaub et al.[49] with aerosol particle pH varied over a broader range (Figure S9), it is clear that there is not a strong correlation (r = −0.471). Correlation (r) values for all acid and base species are provided in Table S3. Further work expanding the number of species studied and range of pH is needed to fully understand the relationship between aerosol particle pH and the ion interactions that dictate broadness of the vibrational modes corresponding to the species of the acid−base equilibrium systems.

CONCLUSIONS

In this study, pH was determined for individual laboratory generated aerosol particles of varying composition at ambient conditions using Raman microspectroscopic measurements of acid and conjugate base species and the extended Debye−Hückel relationship. The acid−base equilibrium systems tested included two inorganic (nitric acid/nitrate and bicarbonate/carbonate), two organic (bioxalate/oxalate and acetic acid/acetate), as well as a mixture of both inorganic and organic (bisulfate/sulfate and bioxalate/oxalate). In addition to aerosol particle pH measurements, this study explored gas-particle partitioning of volatile acid species and a few aspects of ion behavior in relation to particle pH. Nitric acid and acetic acid were found to partition from the particle to the gas phase due to increased surface to volume ratios and did so more than the other acid species because of their higher volatility. In terms of the impact of organic and inorganic components on ionic strength and H^+ activity, the inorganic particles had larger, more variable ionic strength with smaller, less change in the H^+ activity coefficient, while the organic particles had larger, more variable H^+ activity coefficient values with smaller, less change in ionic strength. Finally, the relationship between particle pH and peak broadness was explored and revealed unique trends in peak broadness with changing pH for both inorganic and organic acid and base species. These results show the potential for direct measurement of pH and ion behavior in individual aerosol particles and will enable future studies of more chemically complex particles, including ambient aerosol, which will improve understanding of their pH-dependent chemical processes and climate-relevant properties.

ASSOCIATED CONTENT

Supporting Information

The Supporting Information is available free of charge on the ACS Publications website at DOI: 10.1021/acs.jpca.7b05261.

Table of concentration of bulk solutions and ion ratios used in calculations, calibration curves for all systems, Raman spectra of oxalic acid, bioxalate, and oxalate standards, comparison of bulk solution and particle spectra for oxalate and oxalate−sulfate mixed systems, table of correlation values for aerosol particle pH to fwhm, and comparison of aerosol particle pH as a function of fwhm for sulfate and bisulfate to previous studies (PDF)

AUTHOR INFORMATION

Corresponding Author

*E-mail: aulta@umich.edu.

ORCID

Cari S. Dutcher: 0000-0003-4325-9197

Andrew P. Ault: 0000-0002-7313-8559

Notes

The authors declare no competing financial interest.

ACKNOWLEDGMENTS

This work was supported by the National Science Foundation Grant No. CAREER-1654149 (Ault) and No. CAREER-1554936 (Dutcher), startup funds from the Univ. of Michigan, and RLC was supported by the Susan Lipschutz Fellowship Award from the Univ. of Michigan Rackham Graduate School.

REFERENCES

(1) Prather, K. A.; Hatch, C. D.; Grassian, V. H. Analysis of atmospheric aerosols. *Annu. Rev. Anal. Chem.* **2008**, *1*, 485−514.

(2) Jang, M.; Kamens, R. M. Atmospheric secondary aerosol formation by heterogeneous reactions of aldehydes in the presence of a sulfuric acid aerosol catalyst. *Environ. Sci. Technol.* **2001**, *35* (24), 4758−4766.

(3) Cao, G.; Jang, M. Effects of particle acidity and UV light on secondary organic aerosol formation from oxidation of aromatics in the absence of NOx. *Atmos. Environ.* **2007**, *41* (35), 7603−7613.

(4) Tan, Y.; Perri, M. J.; Seitzinger, S. P.; Turpin, B. J. Effects of precursor concentration and acidic sulfate in aqueous glyoxal-OH

DOI: 10.1021/acs.jpca.7b05261
J. Phys. Chem. A 2017, 121, 5690−5699

radical oxidation and implications for secondary organic aerosol. *Environ. Sci. Technol.* **2009**, *43* (21), 8105−8112.
(5) Wong, J. P. S.; Lee, A. K. Y.; Abbatt, J. P. D. Impacts of sulfate seed acidity and water content on isoprene secondary organic aerosol formation. *Environ. Sci. Technol.* **2015**, *49* (22), 13215−13221.
(6) Riva, M.; Budisulistiorini, S. H.; Chen, Y.; Zhang, Z.; D'Ambro, E. L.; Zhang, X.; Gold, A.; Turpin, B. J.; Thornton, J. A.; Canagaratna, M. R.; et al. Chemical characterization of secondary organic aerosol from oxidation of isoprene hydroxyhydroperoxides. *Environ. Sci. Technol.* **2016**, *50* (18), 9889−9899.
(7) Lewandowski, M.; Jaoui, M.; Offenberg, J. H.; Krug, J. D.; Kleindienst, T. E. Atmospheric oxidation of isoprene and 1,3-butadiene: influence of aerosol acidity and relative humidity on secondary organic aerosol. *Atmos. Chem. Phys.* **2015**, *15* (7), 3773−3783.
(8) Lin, Y.-H.; Zhang, Z.; Docherty, K. S.; Zhang, H.; Budisulistiorini, S. H.; Rubitschun, C. L.; Shaw, S. L.; Knipping, E. M.; Edgerton, E. S.; Kleindienst, T. E.; et al. Isoprene epoxydiols as precursors to secondary organic aerosol formation: acid-catalyzed reactive uptake studies with authentic compounds. *Environ. Sci. Technol.* **2012**, *46* (1), 250−258.
(9) Riva, M.; Bell, D. M.; Hansen, A.-M. K.; Drozd, G. T.; Zhang, Z.; Gold, A.; Imre, D.; Surratt, J. D.; Glasius, M.; Zelenyuk, A. Effect of organic coatings, humidity and aerosol acidity on multiphase chemistry of isoprene epoxydiols. *Environ. Sci. Technol.* **2016**, *50* (11), 5580−5588.
(10) Gao, S.; Ng, N. L.; Keywood, M.; Varutbangkul, V.; Bahreini, R.; Nenes, A.; He, J.; Yoo, K. Y.; Beauchamp, J. L.; Hodyss, R. P.; et al. Particle phase acidity and oligomer formation in secondary organic aerosol. *Environ. Sci. Technol.* **2004**, *38* (24), 6582−6589.
(11) Jang, M.; Carroll, B.; Chandramouli, B.; Kamens, R. M. Particle growth by acid-catalyzed heterogeneous reactions of organic carbonyls on preexisting aerosols. *Environ. Sci. Technol.* **2003**, *37* (17), 3828−3837.
(12) Surratt, J. D.; Chan, A. W. H.; Eddingsaas, N. C.; Chan, M. N.; Loza, C. L.; Kwan, A. J.; Hersey, S. P.; Flagan, R. C.; Wennberg, P. O.; Seinfeld, J. H. Reactive intermediates revealed in secondary organic aerosol formation from isoprene. *Proc. Natl. Acad. Sci. U. S. A.* **2010**, *107* (15), 6640−6645.
(13) Eddingsaas, N. C.; VanderVelde, D. G.; Wennberg, P. O. Kinetics and products of the acid-catalyzed ring-opening of atmospherically relevant butyl epoxy alcohols. *J. Phys. Chem. A* **2010**, *114* (31), 8106−8113.
(14) Iinuma, Y.; Boge, O.; Kahnt, A.; Herrmann, H. Laboratory chamber studies on the formation of organosulfates from reactive uptake of monoterpene oxides. *Phys. Chem. Chem. Phys.* **2009**, *11* (36), 7985−7997.
(15) Riva, M.; Budisulistiorini, S. H.; Zhang, Z.; Gold, A.; Surratt, J. D. Chemical characterization of secondary organic aerosol constituents from isoprene ozonolysis in the presence of acidic aerosol. *Atmos. Environ.* **2016**, *130*, 5−13.
(16) Rindelaub, J. D.; McAvey, K. M.; Shepson, P. B. The photochemical production of organic nitrates from α-pinene and loss via acid-dependent particle phase hydrolysis. *Atmos. Environ.* **2015**, *100*, 193−201.
(17) Surratt, J. D.; Gomez-Gonzalez, Y.; Chan, A. W. H.; Vermeylen, R.; Shahgholi, M.; Kleindienst, T. E.; Edney, E. O.; Offenberg, J. H.; Lewandowski, M.; Jaoui, M.; et al. Organosulfate formation in biogenic secondary organic aerosol. *J. Phys. Chem. A* **2008**, *112* (36), 8345−8378.
(18) Rindelaub, J. D.; Borca, C. H.; Hostetler, M. A.; Slade, J. H.; Lipton, M. A.; Slipchenko, L. V.; Shepson, P. B. The acid-catalyzed hydrolysis of an alpha-pinene-derived organic nitrate: kinetics, products, reaction mechanisms, and atmospheric impact. *Atmos. Chem. Phys.* **2016**, *16* (23), 15425−15432.
(19) Hu, K. S.; Darer, A. I.; Elrod, M. J. Thermodynamics and kinetics of the hydrolysis of atmospherically relevant organonitrates and organosulfates. *Atmos. Chem. Phys.* **2011**, *11* (16), 8307−8320.
(20) Prenni, A. J.; DeMott, P. J.; Kreidenweis, S. M. Water uptake of internally mixed particles containing ammonium sulfate and dicarboxylic acids. *Atmos. Environ.* **2003**, *37* (30), 4243−4251.
(21) Ghorai, S.; Laskin, A.; Tivanski, A. V. Spectroscopic evidence of keto−enol tautomerism in deliquesced malonic acid particles. *J. Phys. Chem. A* **2011**, *115* (17), 4373−4380.
(22) Losey, D. J.; Parker, R. G.; Freedman, M. A. pH dependence of liquid−liquid phase separation in organic aerosol. *J. Phys. Chem. Lett.* **2016**, *7* (19), 3861−3865.
(23) You, Y.; Smith, M. L.; Song, M.; Martin, S. T.; Bertram, A. K. Liquid−liquid phase separation in atmospherically relevant particles consisting of organic species and inorganic salts. *Int. Rev. Phys. Chem.* **2014**, *33* (1), 43−77.
(24) Jang, M.; Czoschke, N. M.; Lee, S.; Kamens, R. M. Heterogeneous atmospheric aerosol production by acid-catalyzed particle-phase reactions. *Science* **2002**, *298* (5594), 814−817.
(25) Hennigan, C. J.; Izumi, J.; Sullivan, A. P.; Weber, R. J.; Nenes, A. A critical evaluation of proxy methods used to estimate the acidity of atmospheric particles. *Atmos. Chem. Phys.* **2015**, *15* (5), 2775−2790.
(26) Guo, H.; Xu, L.; Bougiatioti, A.; Cerully, K. M.; Capps, S. L.; Hite, J. R., Jr; Carlton, A. G.; Lee, S. H.; Bergin, M. H.; Ng, N. L.; et al. Fine-particle water and pH in the southeastern United States. *Atmos. Chem. Phys.* **2015**, *15* (9), 5211−5228.
(27) Guo, H.; Sullivan, A. P.; Campuzano-Jost, P.; Schroder, J. C.; Lopez-Hilfiker, F. D.; Dibb, J. E.; Jimenez, J. L.; Thornton, J. A.; Brown, S. S.; Nenes, A.; et al. Fine particle pH and the partitioning of nitric acid during winter in the northeastern United States. *J. Geophys. Res.-Atmos.* **2016**, *121* (17), 10355−10376.
(28) Guo, H.; Liu, J.; Froyd, K. D.; Roberts, J. M.; Veres, P. R.; Hayes, P. L.; Jimenez, J. L.; Nenes, A.; Weber, R. J. Fine particle pH and gas−particle phase partitioning of inorganic species in Pasadena, California, during the 2010 CalNex campaign. *Atmos. Chem. Phys.* **2017**, *17* (9), 5703−5719.
(29) Liu, M.; Song, Y.; Zhou, T.; Xu, Z.; Yan, C.; Zheng, M.; Wu, Z.; Hu, M.; Wu, Y.; Zhu, T. Fine particle pH during severe haze episodes in northern China. *Geophys. Res. Lett.* **2017**, *44*, 5213.
(30) Weber, R. J.; Guo, H.; Russell, A. G.; Nenes, A. High aerosol acidity despite declining atmospheric sulfate concentrations over the past 15 years. *Nat. Geosci.* **2016**, *9* (4), 282−285.
(31) Fountoukis, C.; Nenes, A. ISORROPIA II: A computationally efficient thermodynamic equilibrium model for K^+-Ca^{2+}-Mg^{2+}-NH_4^{2+}-Na^+-SO_4^{2-}-NO_3^--Cl^--H_2O aerosols. *Atmos. Chem. Phys.* **2007**, *7* (17), 4639−4659.
(32) Clegg, S. L.; Brimblecombe, P.; Wexler, A. S. Thermodynamic model of the system H^+−NH_4^+−SO_4^{2-}−NO_3^-−H_2O at tropospheric temperatures. *J. Phys. Chem. A* **1998**, *102* (12), 2137−2154.
(33) Wexler, A. S.; Clegg, S. L. Atmospheric aerosol models for systems including the ions H^+, NH_4^+, Na^+, SO_4^{2-}, NO_3^-, Cl^-, Br^-, and H_2O. *J. Geophys. Res.-Atmos.* **2002**, *107* (D14), 1−14.
(34) Keene, W. C.; Pszenny, A. A. P.; Maben, J. R.; Stevenson, E.; Wall, A. Closure evaluation of size-resolved aerosol pH in the New England coastal atmosphere during summer. *J. Geophys. Res.-Atmos.* **2004**, *109* (D23).10.1029/2004JD004801
(35) Young, A. H.; Keene, W. C.; Pszenny, A. A. P.; Sander, R.; Thornton, J. A.; Riedel, T. P.; Maben, J. R. Phase partitioning of soluble trace gases with size-resolved aerosols in near-surface continental air over northern Colorado, USA, during winter. *J. Geophys. Res.-Atmos.* **2013**, *118* (16), 9414−9427.
(36) Perraud, V.; Bruns, E. A.; Ezell, M. J.; Johnson, S. N.; Yu, Y.; Alexander, M. L.; Zelenyuk, A.; Imre, D.; Chang, W. L.; Dabdub, D.; et al. Nonequilibrium atmospheric secondary organic aerosol formation and growth. *Proc. Natl. Acad. Sci. U. S. A.* **2012**, *109* (8), 2836−2841.
(37) O'Brien, R. E.; Neu, A.; Epstein, S. A.; MacMillan, A. C.; Wang, B. B.; Kelly, S. T.; Nizkorodov, S. A.; Laskin, A.; Moffet, R. C.; Gilles, M. K. Physical properties of ambient and laboratory-generated secondary organic aerosol. *Geophys. Res. Lett.* **2014**, *41* (12), 4347−4353.

DOI: 10.1021/acs.jpca.7b05261
J. Phys. Chem. A 2017, 121, 5690−5699

(38) Virtanen, A.; Joutsensaari, J.; Koop, T.; Kannosto, J.; Yli-Pirila, P.; Leskinen, J.; Makela, J. M.; Holopainen, J. K.; Poeschl, U.; Kulmala, M.; et al. An amorphous solid state of biogenic secondary organic aerosol particles. *Nature* **2010**, *467* (7317), 824−827.
(39) Shiraiwa, M.; Li, Y.; Tsimpidi, A. P.; Karydis, V. A.; Berkemeier, T.; Pandis, S. N.; Lelieveld, J.; Koop, T.; Pöschl, U. Global distribution of particle phase state in atmospheric secondary organic aerosols. *Nat. Commun.* **2017**, *8*, 15002.
(40) Jang, M.; Cao, G.; Paul, J. Colorimetric particle acidity analysis of secondary organic aerosol coating on submicron acidic aerosols. *Aerosol Sci. Technol.* **2008**, *42* (6), 409−420.
(41) Keene, W. C.; Pszenny, A. A. P.; Maben, J. R.; Sander, R. Variation of marine aerosol acidity with particle size. *Geophys. Res. Lett.* **2002**, *29* (7), 5−1−5-4.
(42) Feng, J. L.; Guo, Z. G.; Zhang, T. R.; Yao, X. H.; Chan, C. K.; Fang, M. Source and formation of secondary particulate matter in PM2.5 in Asian continental outflow. *J. Geophys. Res.-Atmos.* **2012**, *117* (D3).10.1029/2011JD016400
(43) Metzger, S.; Mihalopoulos, N.; Lelieveld, J. Importance of mineral cations and organics in gas-aerosol partitioning of reactive nitrogen compounds: case study based on MINOS results. *Atmos. Chem. Phys.* **2006**, *6* (9), 2549−2567.
(44) Trebs, I.; Metzger, S.; Meixner, F. X.; Helas, G.; Hoffer, A.; Rudich, Y.; Falkovich, A. H.; Moura, M. A. L.; da Silva, R. S.; Artaxo, P.; et al. The NH_4^+-NO_3^--Cl^--SO_4^{2-}-H_2O aerosol system and its gas phase precursors at a pasture site in the Amazon Basin: How relevant are mineral cations and soluble organic acids? *J. Geophys. Res.-Atmos.* **2005**, *110* (D7).
(45) Kerminen, V.-M.; Hillamo, R.; Teinilä, K.; Pakkanen, T.; Allegrini, I.; Sparapani, R. Ion balances of size-resolved tropospheric aerosol samples: implications for the acidity and atmospheric processing of aerosols. *Atmos. Environ.* **2001**, *35* (31), 5255−5265.
(46) Zhang, Q.; Jimenez, J. L.; Worsnop, D. R.; Canagaratna, M. A case study of urban particle acidity and its influence on secondary organic aerosol. *Environ. Sci. Technol.* **2007**, *41* (9), 3213−3219.
(47) Pathak, R. K.; Yao, X. H.; Chan, C. K. Sampling artifacts of acidity and ionic species in PM2.5. *Environ. Sci. Technol.* **2004**, *38* (1), 254−259.
(48) Pathak, R. K.; Wu, W. S.; Wang, T. Summertime PM2.5 ionic species in four major cities of China: nitrate formation in an ammonia-deficient atmosphere. *Atmos. Chem. Phys.* **2009**, *9* (5), 1711−1722.
(49) Rindelaub, J. D.; Craig, R. L.; Nandy, L.; Bondy, A. L.; Dutcher, C. S.; Shepson, P. B.; Ault, A. P. Direct measurement of pH in individual particles via Raman microspectroscopy and variation in acidity with relative humidity. *J. Phys. Chem. A* **2016**, *120* (6), 911−917.
(50) Ault, A. P.; Axson, J. L. Atmospheric aerosol chemistry: Spectroscopic and microscopic advances. *Anal. Chem.* **2017**, *89* (1), 430−452.
(51) Ault, A. P.; Zhao, D.; Ebben, C. J.; Tauber, M. J.; Geiger, F. M.; Prather, K. A.; Grassian, V. H. Raman microspectroscopy and vibrational sum frequency generation spectroscopy as probes of the bulk and surface compositions of size-resolved sea spray aerosol particles. *Phys. Chem. Chem. Phys.* **2013**, *15* (17), 6206−6214.
(52) Creamean, J. M.; Axson, J. L.; Bondy, A. L.; Craig, R. L.; May, N. W.; Shen, H.; Weber, M. H.; Pratt, K. A.; Ault, A. P. Changes in precipitating snow chemistry with location and elevation in the California Sierra Nevada. *J. Geophys. Res.-Atmos.* **2016**, *121* (12), 7296−7309.
(53) Craig, R. L.; Bondy, A. L.; Ault, A. P.; Computer-controlled Raman microspectroscopy (CC-Raman): A method for the rapid characterization of individual atmospheric aerosol particles. *Aerosol Sci. Technol.* 2017, *51*, 10.1080/02786826.2017.1337268
(54) Craig, R. L.; Bondy, A. L.; Ault, A. P. Surface enhanced Raman spectroscopy enables observations of previously undetectable secondary organic aerosol components at the individual particle level. *Anal. Chem.* **2015**, *87* (15), 7510−7514.
(55) Ebben, C. J.; Ault, A. P.; Ruppel, M. J.; Ryder, O. S.; Bertram, T. H.; Grassian, V. H.; Prather, K. A.; Geiger, F. M. Size-Resolved Sea Spray Aerosol Particles Studied by Vibrational Sum Frequency Generation. *J. Phys. Chem. A* **2013**, *117* (30), 6589−6601.
(56) Ault, A. P.; Guasco, T. L.; Baltrusaitis, J.; Ryder, O. S.; Trueblood, J. V.; Collins, D. B.; Ruppel, M. J.; Cuadra-Rodriguez, L. A.; Prather, K. A.; Grassian, V. H. Heterogeneous reactivity of nitric acid with nascent sea spray aerosol: large differences observed between and within individual particles. *J. Phys. Chem. Lett.* **2014**, *5*, 2493−2500.
(57) Wren, S. N.; Donaldson, D. J. How does deposition of gas phase species affect pH at frozen salty interfaces? *Atmos. Chem. Phys.* **2012**, *12* (21), 10065−10073.
(58) Wren, S. N.; Donaldson, D. J. Laboratory study of pH at the air−ice interface. *J. Phys. Chem. C* **2012**, *116* (18), 10171−10180.
(59) Lide, D. R. *CRC Handbook of Chemistry and Physics: A Ready-Reference Book of Chemical and Physical Data;* CRC Press: Boca Raton, FL, 2009.
(60) Hood, G. C.; Redlich, O.; Reilly, C. A. Ionization of strong electrolytes. III. Proton magnetic resonance in nitric, perchloric, and hydrochloric acids. *J. Chem. Phys.* **1954**, *22* (12), 2067−2071.
(61) Grassian, V. H. Particle chemistry in the environment: Challenges and opportunities. *J. Phys. Chem. Lett.* **2015**, *6* (19), 3880−3881.
(62) Laliberte, M. A model for calculating the heat capacity of aqueous solutions, with updated density and viscosity data. *J. Chem. Eng. Data* **2009**, *54* (6), 1725−1760.
(63) Clegg, S. L.; Simonson, J. M. A BET model of the thermodynamics of aqueous multicomponent solutions at extreme concentration. *J. Chem. Thermodyn.* **2001**, *33* (11), 1457−1472.
(64) Garrels, R. M.; Christ, C. L. *Solutions, Minerals, and Equilibria;* Harper & Row Publishers, Inc.: New York, NY, 1965.
(65) Kielland, J. Individual activity coefficients of ions in aqueous solutions. *J. Am. Chem. Soc.* **1937**, *59* (9), 1675−1678.
(66) Vargas Jentzsch, P.; Kampe, B.; Ciobota, V.; Roesch, P.; Popp, J. Inorganic salts in atmospheric particulate matter: Raman spectroscopy as an analytical tool. *Spectrochim. Acta, Part A* **2013**, *115*, 697−708.
(67) Waterland, M. R.; Stockwell, D.; Kelley, A. M. Symmetry breaking effects in NO_3^-: Raman spectra of nitrate salts and ab initio resonance Raman spectra of nitrate−water complexes. *J. Chem. Phys.* **2001**, *114* (14), 6249−6258.
(68) Wren, S. N.; Donaldson, D. J. Glancing-angle Raman study of nitrate and nitric acid at the air−aqueous interface. *Chem. Phys. Lett.* **2012**, *522*, 1−10.
(69) Ratcliffe, C. I.; Irish, D. E. Vibrational spectral studies of solutions at elevated temperatures and pressures. VII. Raman spectra and dissociation of nitric acid. *Can. J. Chem.* **1985**, *63* (12), 3521−3525.
(70) Dutcher, C. S.; Ge, X.; Wexler, A. S.; Clegg, S. L. An isotherm-based thermodynamic model of multicomponent aqueous solutions, applicable over the entire concentration range. *J. Phys. Chem. A* **2013**, *117* (15), 3198−3213.
(71) Rudolph, W. W.; Irmer, G.; Konigsberger, E. Speciation studies in aqueous HCO_3^--CO_3^{2-} solutions. A combined Raman spectroscopic and thermodynamic study. *Dalton Trans.* **2008**, *7*, 900−908.
(72) Magid, E.; Turbeck, B. O. The rates of the spontaneous hydration of CO_2 and the reciprocal reaction in neutral aqueous solutions between 0° and 38°. *Biochim. Biophys. Acta, Gen. Subj.* **1968**, *165* (3), 515−524.
(73) de Villepin, J.; Novak, A. Vibrational spectra of and isotope effect in hydrogen bonded potassium hydrogen oxalate. *Spectrosc. Lett.* **1971**, *4* (1−2), 1−8.
(74) Gruen, E. C.; Plane, R. A. Raman study of aqueous metal oxalate complexes and related oxalates. *Inorg. Chem.* **1967**, *6* (6), 1123−1127.
(75) Ito, K.; Bernstein, H. J. The vibrational spectra of the formate, acetate, and oxalate ions. *Can. J. Chem.* **1956**, *34* (2), 170−178.
(76) Hibben, J. H. The raman spectra of oxalic acid. *J. Chem. Phys.* **1935**, *3* (11), 675−679.
(77) Ng, J. B.; Shurvell, H. F. Application of factor analysis and band contour resolution techniques to the Raman spectra of acetic acid in aqueous solution. *J. Phys. Chem.* **1987**, *91* (2), 496−500.

DOI: 10.1021/acs.jpca.7b05261
J. Phys. Chem. A 2017, 121, 5690−5699

(78) Nakabayashi, T.; Kosugi, K.; Nishi, N. Liquid structure of acetic acid studied by raman spectroscopy and ab initio molecular orbital calculations. *J. Phys. Chem. A* **1999**, *103* (43), 8595−8603.
(79) Nishi, N.; Nakabayashi, T.; Kosugi, K. Raman spectroscopic study on acetic acid clusters in aqueous solutions: dominance of acid−acid association producing microphases. *J. Phys. Chem. A* **1999**, *103* (50), 10851−10858.
(80) Sander, R. Compilation of Henry's law constants (version 4.0) for water as solvent. *Atmos. Chem. Phys.* **2015**, *15* (8), 4399−4981.
(81) Laskin, A.; Moffet, R. C.; Gilles, M. K.; Fast, J. D.; Zaveri, R. A.; Wang, B.; Nigge, P.; Shutthanandan, J. Tropospheric chemistry of internally mixed sea salt and organic particles: Surprising reactivity of NaCl with weak organic acids. *J. Geophys. Res.-Atmos.* **2012**, *117* (D15).10.1029/2012JD017743
(82) Larkin, P. *Infrared and Raman Spectroscopy; Principles and Spectral Interpretation;* Elsevier, 2011.

DOI: 10.1021/acs.jpca.7b05261
J. Phys. Chem. A 2017, 121, 5690−5699